Check for updates

Defect chemistry and transport properties of perovskite-type oxides La$_{1-x}$Ca$_x$FeO$_{3-\delta}$†

Jia Song, ‡[a] Shaochen Zhu, [a] De Ning§[b] and Henny J. M. Bouwmeester *[acd]

Structural evolution, electrical conductivity, oxygen nonstoichiometry and oxygen transport properties of perovskite-type oxides La$_{1-x}$Ca$_x$FeO$_{3-\delta}$ (x = 0.05, 0.10, 0.15, 0.20, 0.30 and 0.40) are investigated. All investigated compositions exhibit, under ambient air, a phase transition from room-temperature orthorhombic (space group *Pbnm*) to rhombohedral (space group $R\bar{3}c$) at elevated temperature. The transition temperature is found to decrease gradually from 900 °C for x = 0.05 to 625 °C for x = 0.40. Analysis of the data of oxygen nonstoichiometry obtained by thermogravimetry shows that under the given experimental conditions the Ca dopant is predominantly compensated by formation of electron holes rather than by oxygen vacancies. Maximum electrical conductivity under air is found for the composition with x = 0.30 (123 S cm^{-1} at 650 °C). Analysis of the temperature dependence of the mobility of the electron holes in terms of Emin–Holstein's theory indicates that small polaron theory fails for the compositions with high Ca contents x = 0.30 and x = 0.40. This is tentatively explained by the increased delocalization of charge carriers with increasing Ca dopant concentration. The oxygen transport properties of La$_{1-x}$Ca$_x$FeO$_{3-\delta}$ in the range 650–900 °C are evaluated using the electrical conductivity relaxation (ECR) technique. Combined with data of oxygen non-stoichiometry, the obtained results enable calculation of the oxygen vacancy diffusion coefficient and associated ionic conductivity. Both parameters increase with increasing Ca content in La$_{1-x}$Ca$_x$FeO$_{3-\delta}$, while it is found that the effective migration barrier for oxygen diffusion decreases with decreasing oxygen vacancy formation enthalpy.

1. Introduction

Mixed ionic–electronic conducting oxides are extensively investigated for potential application as air electrode in reversible solid oxide cells (RSOCs) that can be operated either as a solid oxide fuel cell (SOFC) or as a solid electrolyte electrolysis cell (SOEC).[1–3] The most popular electrodes considered to date are the perovskite-structured oxides La$_{0.6}$Sr$_{0.4}$CoO$_{3-\delta}$

[a]Electrochemistry Research Group, Membrane Science and Technology, MESA+ Institute for Nanotechnology, University of Twente, P.O. Box 217, 7500 AE, Enschede, The Netherlands. E-mail: h.j.m.bouwmeester@utwente.nl

[b]Helmholtz-Zentrum Berlin für Materialien und Energie, Hahn-Meitner-Platz 1, 14109 Berlin, Germany

[c]CAS Key Laboratory of Materials for Energy Conversion, Department of Materials Science and Engineering, University of Science and Technology of China, Hefei, 230026, P. R. China

[d]Forschungszentrum Jülich GmbH, Institute of Energy and Climate Research-IEK-1, Leo-Brandt-Str. 1, D-52425, Jülich, Germany

† Electronic supplementary information (ESI) available. See DOI: 10.1039/d0ta07508f

‡ Separation and Conversion Technology, Flemish Institute for Technological Research (VITO), Boeretang 200, Mol 2400, Belgium

§ Center for Information Photonics and Energy Materials, Shenzhen Institutes of Advanced Technology (SIAT), Chinese Academy of Sciences, Shenzhen 518055, P. R. China

(LSC) and La$_{0.6}$Sr$_{0.4}$Co$_{0.2}$Fe$_{0.8}$O$_{3-\delta}$ (LSCF), though many other compositions and structure types are currently being investigated.[4] Oxygen ion transport in these oxides is mediated *via* a vacancy mechanism. A-site substitution of trivalent lanthanum with divalent strontium in the ABO$_3$ perovskite oxides serves to create oxygen vacancies and, hence, to enhance oxygen ionic conductivity. A drawback in the case of above compositions is the clear mismatch between the ionic radii of host and dopant ions, La^{3+} (XII) = 1.36 Å and Sr^{2+} (XII) = 1.44 Å, which is believed to be the cause of segregation of Sr^{2+} ions to the grain boundaries and to the surface. The latter has a detrimental effect on the surface oxygen exchange kinetics.[5–8] Apart from this, the long-term thermodynamic stability of materials under actual operating conditions is an issue. The poor stability of cobalt-containing perovskites under reducing atmospheres, reactivity towards commonly used electrolytes and – last but not least – the high price of cobalt have urged researchers to explore cobalt-free mixed conducting electrodes with high electrocatalytic activity.[9–11]

In recent studies by Berger *et al.*,[12,13] La$_{0.8}$Ca$_{0.2}$FeO$_{3-\delta}$ (LCF82) has been put forward as a promising electrode for RSOCs. The choice for calcium (Ca^{2+} (XII) = 1.34 Å) rather than strontium not only reduces the mismatch between host and dopant ions, but also the lower basicity of Ca^{2+} compared to that

of Sr^{2+} ions reduces vulnerability towards carbonation and, hence, surface degradation upon contact with CO_2. The thermal expansion coefficient of LCF82 is found in perfect match with that of state-of-the-art electrolytes,[12] whereas the material shows electrical conductivities in usual ranges of temperature and oxygen partial pressure (pO_2) in excess of 100 S cm^{-1}, which is often regarded as the threshold value for use as electrode.[14] It is further found that LCF82 exhibits high surface exchange and chemical diffusion coefficients with values exceeding those of state-of-the-art materials like LSC and LSCF.[12]

In our preceding work, investigating the influence of the earth–alkaline–metal dopant on structure, electrical and oxygen transport of $La_{0.6}A_{0.4}FeO_{3-\delta}$ (A = Ca, Sr, Ba), we found that the kinetic parameters for $La_{0.6}Ca_{0.4}FeO_{3-\delta}$ (LCF64) resemble those of $La_{0.6}Sr_{0.4}FeO_{3-\delta}$ (LSF64).[15] Compared to extensive reports in literature on structure, electrical conductivity and oxygen transport properties of $La_{1-x}Sr_xFeO_{3-\delta}$ (LSF),[16–21] only a few reports are available on selected compositions in the series $La_{1-x}Ca_xFeO_{3-\delta}$.[12,22,23] This prompted us to conduct a more systematic study. In this study, the electrical conductivity and oxygen transport properties of $La_{1-x}Ca_xFeO_{3-\delta}$ (x = 0.05, 0.10, 0.15, 0.20, 0.30 and 0.40) are investigated by means of electrical conductivity relaxation (ECR). Thermal evolution of the crystal structure and oxygen nonstoichiometry of the materials are investigated by high-temperature X-ray diffraction (HT-XRD) and thermogravimetric analysis (TGA).

2. Experimental

2.1 Sample preparation

Powders of $La_{1-x}Ca_xFeO_{3-\delta}$ (x = 0.05, 0.10, 0.15, 0.20, 0.30 and 0.40) were prepared *via* a modified Pechini method, as described elsewhere.[24] Stoichiometric amounts of $La(NO_3)_3$·$6H_2O$ (Alfa Aesar, 99.9%), $Ca(NO_3)_2$·$4H_2O$ (Sigma-Aldrich, 99%) and $Fe(NO_3)_3$·$9H_2O$ (Sigma-Aldrich, ≥98%) were dissolved in water followed by the addition of $C_{10}H_{16}N_2O_8$ (EDTA, Sigma-Aldrich, >99%) and $C_6H_8O_7$ (citric acid, Alfa Aesar, >99.5%) as chelating agents. The pH of the solution was adjusted to 7 using concentrated NH_4OH (Sigma-Aldrich, 30 w/v%). After evaporation of the water, the foam-like gel reached self-ignition at around 350 °C. The obtained raw ashes were calcined at 900 °C for 5 h, using heating/cooling rates of 5 °C min^{-1}. The chemical composition of the powders was checked by X-ray fluorescence (XRF) using a Philips PW1480 apparatus. The obtained powders were pelletized by uniaxial pressing at 25 MPa followed by isostatic pressing at 400 MPa for 2 min. Subsequently, the pellets were sintered at 1120 °C for 5 h in air with heating/cooling rates of 2 °C min^{-1}. The relative density of the pellets was above 94% of their theoretical value as measured by Archimedes' method.

2.2 Characterization

The calcined powders were studied by room-temperature X-ray diffraction (XRD, D2 PHASER, Bruker) with Cu $K\alpha_1$ radiation (λ = 1.54060 Å) in air. Data were collected in a step-scan mode over the 2θ range 20–90 °C with a step size of 0.01° and

a counting time of 8 s. The thermal evolution of the structures was investigated using high-temperature X-ray diffraction (HT-XRD, D8 Advance, Bruker) in air from 600 °C to 1000 °C with 25 °C intervals. The sample was heated to the desired temperature with a heating rate of 25 °C min^{-1}, followed by a dwell of 15 min to ensure equilibration. XRD patterns were recorded in the 2θ range of 20–90° with a step size of 0.015° and a counting time of 1.3 s. The FullProf software package was used for Rietveld refinements of the patterns.[25]

The oxygen nonstoichiometry of the samples was determined by thermogravimetric analysis (TGA, Netsch STA F3 Jupiter). Data were collected during cooling from 900 °C to 650 °C, with intervals of 25 °C and a dwell time of 30 min at each temperature before data acquisition. The measurements were conducted in oxygen–nitrogen mixtures containing either 4.5%, 10%, 21%, 42% or 90% of O_2, corresponding to the pO_2 values maintained during ECR experiments (see below). Prior to data collection, the powder was heated under 4.5% O_2 to 900 °C, with a heating rate of 20 °C min^{-1} and a dwell time of at least 2.5 h, in order to remove impurities like adsorbed water and CO_2. Following prior studies on $La_{1-x}Sr_xFeO_{3-\delta}$ ($0 \le x \le 0.6$),[17] all compositions in the present study were considered to be stoichiometric ($\delta = 0$) at a pO_2 of 0.21 atm below 150 °C.

Samples for electrical conductivity relaxation (ECR) measurements were prepared by grinding and cutting dense sintered pellets to planar-sheet shaped samples with approximate dimensions $12 \times 5 \times 0.5$ mm^3. The sample surface was polished using diamond polishing discs (JZ Primo, Xinhui China) down to 0.5 μm. A four-probe DC method was used to collect data of electrical conductivity. Two gold wires (Alfa Aesar, 99.999%, Ø = 0.25 mm) were wrapped around both ends of the sample for current supply. Two additional gold wires were wrapped 1 mm remote from the current electrodes to act as voltage probes. To ensure good contact between the gold wires and the sample, sulphur-free gold paste (home-made) was applied on the sample surface directly underneath the gold wires. Finally, the sample was annealed at 950 °C in air for 1 h to sinter the gold paste and thermally cure the polished sample surface. Data of the transient electrical conductivity was collected following oxidation and reduction step changes in pO_2 between 0.100 and 0.210 bar. Measurements were conducted following stepwise cooling from 900 °C to 650 °C with intervals of 25 °C, heating/cooling rates of 10 °C min^{-1} and a dwell time of 60 min at each temperature before data acquisition. The chemical diffusion coefficient D_{chem} and the surface exchange coefficient k_{chem} were determined by fitting the transient conductivity to the appropriate solution of Fick's second law using a non-linear least-squares program based on the Levenberg–Marquardt algorithm. Detailed descriptions of the ECR technique and the model used for data fitting are given elsewhere.[19,26]

3. Results and discussion

3.1 Crystal structure

Fig. 1 shows the room temperature XRD patterns of $La_{1-x}Ca_x$-$FeO_{3-\delta}$ (x = 0.05, 0.10, 0.15, 0.20, 0.30 and 0.40). All patterns

This journal is © The Royal Society of Chemistry 2021
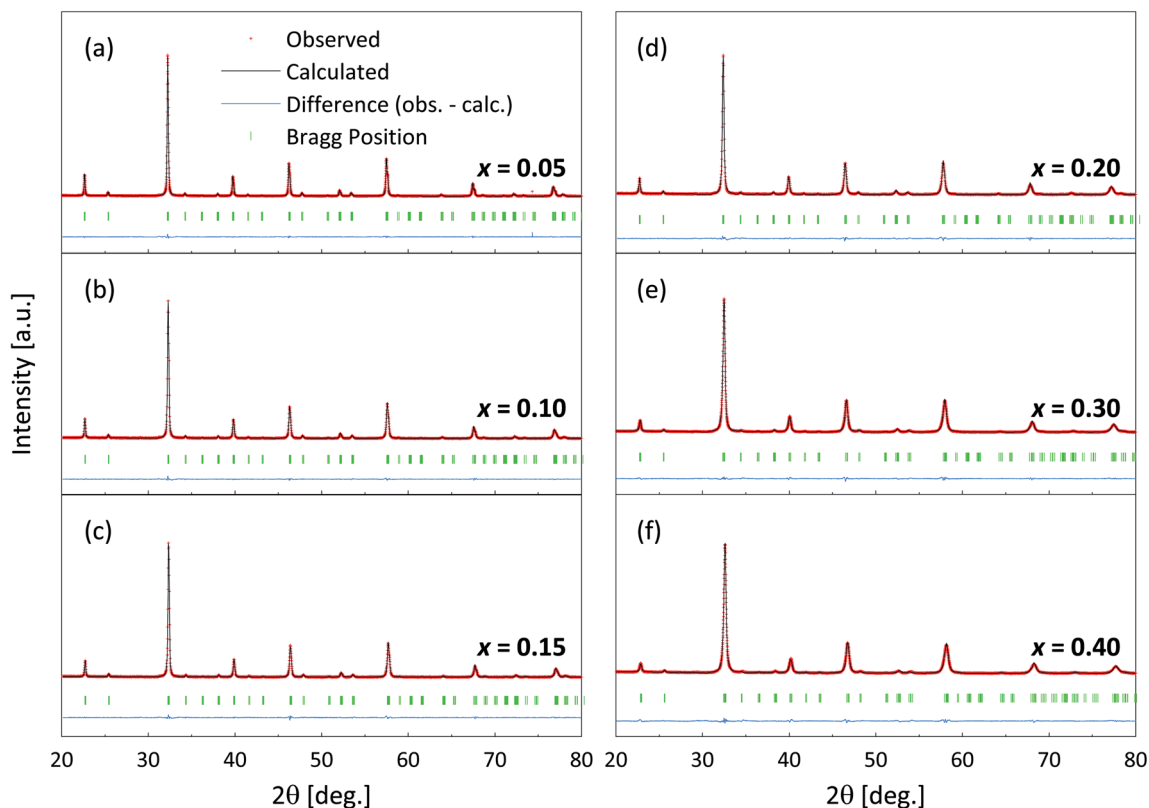
J. Mater. Chem. A, 2021, **9**, 974–989 | **975**

Fig. 1 Measured (red symbols) and calculated (black lines) of XRD powder patterns of $La_{1-x}Ca_xFeO_{3-\delta}$ for (a) $x = 0.05$, (b) $x = 0.10$, (c) $x = 0.15$, (d) $x = 0.20$, (e) $x = 0.30$ and (f) $x = 0.40$. Data were recorded at room temperature in ambient air. The calculated positions of Bragg peaks and the residual plots are given under the patterns. Data for $x = 0.40$ were taken from our previous study.[15]

could be fitted using orthorhombic space group *Pbnm*. Corresponding lattice parameters and reliability factors from Rietveld refinements are listed in Table 1. Other structural parameters obtained from the refinements are listed in Table S1.† No impurity peaks are found in the patterns, suggesting that all compositions are single phase. The chemical composition of the powders appeared to be in good agreement with the intended nominal composition as was checked by XRF (see Fig. S1†).

As is shown in Fig. 2, the lattice parameters show a clear negative dependence on Ca content, which suggests at first glance formation of Fe^{4+} (0.585 Å (XI)) as the primary compensating defect, noting that the Fe^{4+} ion has a smaller radius than Fe^{3+} (0.645 Å (XI) – high spin). The degree of electronic *versus*

ionic compensation of the Ca dopant in $La_{1-x}Ca_xFeO_{3-\delta}$ is further discussed below. The quoted ionic radii are taken from Shannon's compilation.[27] In general, a good agreement is found between the lattice parameters from this study and those of similar compositions reported by Price *et al.*[22]

The temperature dependences of the pseudo-cubic lattice parameters obtained from Rietveld refinements of the HT-XRD patterns of samples $La_{1-x}Ca_xFeO_{3-\delta}$ are listed in Fig. 3. These give evidence of a structural phase transition from orthorhombic to rhombohedral (space group $R\bar{3}c$), *i.e.*, a slightly distorted cubic structure, occurring in all of the investigated compositions. The degree of distortion is found to decrease with temperature and Ca content. For example, at 1000 °C, the

Table 1 Lattice parameters and reliability factors obtained from Rietveld refinements of room temperature XRD diffractograms of $La_{1-x}Ca_x$-$FeO_{3-\delta}$ (space group *Pbnm*). The numbers in parentheses denote standard deviations in units of the least significant digits

	$x = 0.05$	$x = 0.10$	$x = 0.15$	$x = 0.20$	$x = 0.30$	$x = 0.40$
$a/Å$	5.54765(4)	5.54089(11)	5.52984(11)	5.52167(15)	5.50262(10)	5.48822(12)
$b/Å$	5.55664(3)	5.54966(8)	5.54068(9)	5.53475(13)	5.52552(9)	5.51710(15)
$c/Å$	7.84294(5)	7.83187(13)	7.81634(14)	7.80452(19)	7.77789(13)	7.75721(17)
$V/Å^3$	241.769(2)	240.831(4)	239.485(4)	238.514(5)	236.486(4)	234.881(4)
$R_{wp}/\%$	4.96	6.33	7.33	7.19	5.72	6.29
$R_{exp}/\%$	1.99	4.55	4.89	4.06	2.41	2.52
$R_{Bragg}/\%$	1.275	1.769	1.868	2.050	1.875	2.237
χ^2	6.22	1.93	2.25	3.14	5.65	6.23

976 | *J. Mater. Chem. A*, 2021, **9**, 974–989

This journal is © The Royal Society of Chemistry 2021

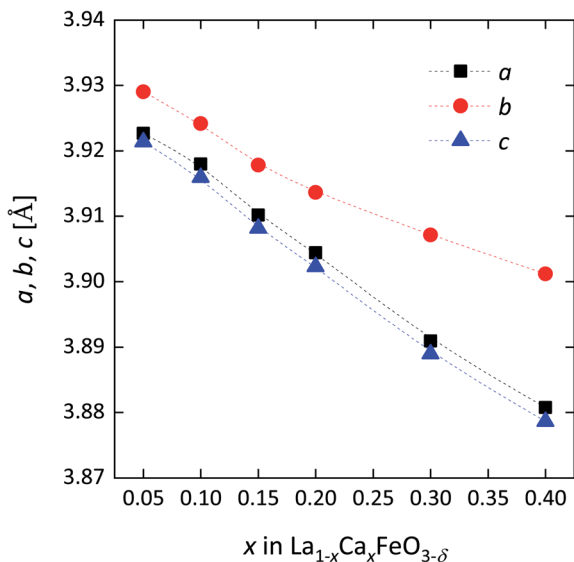**Fig. 2** Lattice parameters of $La_{1-x}Ca_xFeO_{3-\delta}$ as a function of x from Rietveld refinements of room temperature XRD powder patterns (*cf.* Fig. 1). Orthorhombic (*Pbnm*) lattice parameters for LCF phases are presented as pseudo-cubic lattice parameters, calculated using $a = a_{ortho}/\sqrt{2}$, $b = b_{ortho}/\sqrt{2}$ and $c = c_{ortho}/2$.

rhombohedral angle decreases in the order $x = 0.05$ (60.31°) $> x = 0.10$ (60.28°) $> x = 0.15$ (60.24°) $> x = 0.20$ (60.19°) $> x = 0.30$ (60.11°) $> x = 0.40$ (60.09°), noting that the value of 60° corresponds to ideal cubic symmetry. The observed transition temperatures are listed in Table 2 and compared, as far as available, with those found using differential scanning calorimetry (DSC) by Price *et al.*[22] The lowering of the transition temperature with Ca content can be explained by the concomitant decrease of the deformation of the perovskite structure.

3.2 Oxygen nonstoichiometry

The oxygen nonstoichiometry (δ) of $La_{1-x}Ca_xFeO_{3-\delta}$ was investigated as a function of temperature and pO_2 by thermogravimetric analysis. A typical measurement scheme is shown in Fig. S2.† Corresponding data plotted as a function of pO_2, at different temperatures, for each of the compositions are shown in Fig. 4. As can be inferred from these figures, δ, at a given temperature and pO_2, increases with increasing Ca mole fraction.

Starting point in our discussion of the defect chemistry of $La_{1-x}Ca_xFeO_{3-\delta}$ is the model developed by Mizusaki *et al.*[16–18] for $La_{1-x}Sr_xFeO_{3-\delta}$. Assuming localized and non-interacting defects, the oxidation reaction is described, in Kröger–Vink notation, as

$$O_2 + 2V_O^{\bullet\bullet} + 4Fe_{Fe}^\times \leftrightarrows 2O_O^\times + 4Fe_{Fe}^\bullet \tag{1}$$
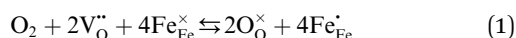
with equilibrium constant in the ideal solution approximation

$$K_{ox} = \frac{[O_O^\times]^2 [Fe_{Fe}^\bullet]^4}{pO_2 [V_O^{\bullet\bullet}]^2 [Fe_{Fe}^\times]^4} \tag{2}$$

Under oxidizing conditions, $V_O^{\bullet\bullet}$ coexists with $Fe_{Fe}^\bullet$, which is reflected in the reduced charge neutrality equation corresponding to this region, which reads

$$[Ca_{La}'] = 2[V_O^{\bullet\bullet}] + [Fe_{Fe}^\bullet] \tag{3}$$

showing that the partial substitution of La^{3+} ions by Ca^{2+} is charge compensated by the formation of localized electron holes $Fe_{Fe}^\bullet$ (Fe^{4+}) and oxygen vacancies $V_O^{\bullet\bullet}$. Eqn (3) ignores the presence of localized electrons Fe_{Fe}' (Fe^{2+}), arising from disproportionation of two Fe^{3+} ions in Fe^{2+} and Fe^{4+},

$$2Fe_{Fe}^\times \rightleftharpoons Fe_{Fe}' + Fe_{Fe}^\bullet \tag{4}$$
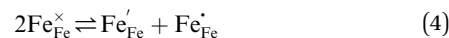
which electronic defects become predominant under reducing conditions, and that of structural vacancies on lanthanum (V_{La}''') and iron (V_{Fe}''') sites. Using eqn (3), the concentration of $Fe_{Fe}^\bullet$ in $La_{1-x}Ca_xFeO_{3-\delta}$ at a given temperature and pO_2 can be calculated from corresponding data of oxygen nonstoichiometry (Fig. 4). Fig. 5 shows the results of such calculations for $pO_2 = 0.1$ atm and $pO_2 = 1$ atm, at 800 °C, from which figure it can be inferred that under the given experimental conditions in each of the compositions electronic compensation of the Ca dopant dominates over ionic compensation.

The use of eqn (2) to describe the equilibrium between oxygen in the gas phase and oxygen in the oxide relies on the assumption that the oxygen incorporation energetics is independent of the concentration of involved point defects, which are further taken to be randomly distributed among available lattice sites. The validity of this assumption in the experimental range of the measurements can be checked by estimating the standard enthalpy change (ΔH_{ox}^0) involved in the oxidation reaction (reaction (1)). The relationship between the standard free Gibbs energy change (ΔG_{ox}^0) and the equilibrium constant (K_{ox}) is

$$\Delta G_{ox}^0 = \Delta H_{ox}^0 - T\Delta S_{ox}^0 = -RT \ln(K_{ox}) \tag{5}$$

where ΔS_{ox}^0 is the standard reaction entropy change of the reaction and R is the universal gas constant. Assuming that ΔH_{ox}^0 is independent of temperature, ΔH_{ox}^0 can be calculated from the slope of $\ln(K_{ox})$ *vs.* $1/T$, according to

$$\ln(K_{ox}) = -\frac{\Delta H_{ox}^0}{RT} + \frac{\Delta S_{ox}^0}{R} \tag{6}$$

which is known as the van 't Hoff equation, while ΔS_{ox}^0 is calculated from the intercept. $\ln(K_{ox})$ *vs.* $1/T$ plots, at constant pO_2, for $La_{0.7}Ca_{0.3}FeO_{3-\delta}$ are shown in Fig. 6a. The observed non-linearity and the observation that different plots are obtained at different pO_2 values indicate that K_{ox} is a non-ideal equilibrium constant. Fig. 6b shows $\ln(K_{ox})$ *vs.* $1/T$ plots, at constant δ, for $La_{0.7}Ca_{0.3}FeO_{3-\delta}$. Distinct from those presented in Fig. 6a, linear plots are obtained, with slopes that are a function of δ. Similar results were obtained for the other compositions investigated in this work. Values of ΔH_{ox}^0 and
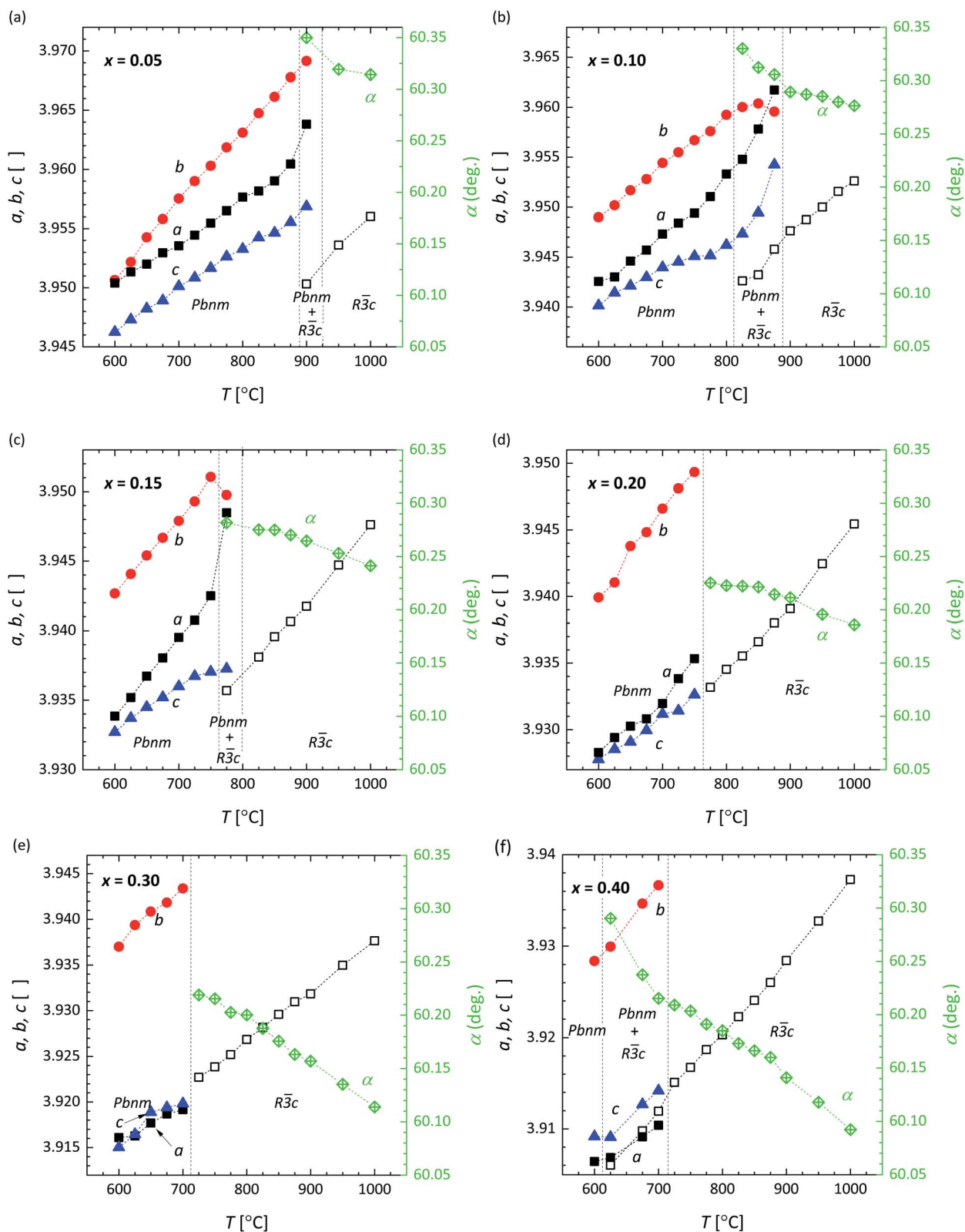
This journal is © The Royal Society of Chemistry 2021

J. Mater. Chem. A, 2021, **9**, 974–989 | **977**

Fig. 3 Lattice parameters of $La_{1-x}Ca_xFeO_{3-\delta}$ for (a) $x = 0.05$, (b) $x = 0.10$, (c) $x = 0.15$, (d) $x = 0.20$, (e) $x = 0.30$ and (f) $x = 0.40$ as a function of temperature from Rietveld refinements of HT-XRD patterns recorded in ambient air. For the orthorhombic (*Pbnm*) structure pseudo-cubic lattice parameters are given, calculated using $a = a_{ortho}/\sqrt{2}$, $b = b_{ortho}/\sqrt{2}$ and $c = c_{ortho}/2$. For the rhombohedral ($R\bar{3}c$) structure, $a = b = c \equiv a$. Data for $x = 0.40$ were taken from our previous study.[15]

978 | *J. Mater. Chem. A*, 2021, **9**, 974–989

This journal is © The Royal Society of Chemistry 2021

Table 2 Comparison of the transition temperature of the orthorhombic-to-rhombohedral phase transition in La$_{1-x}$Ca$_x$FeO$_{3-\delta}$ from HTXRD (this study) with that estimated using differential scanning calorimetry (DSC) by Price et al.[22]

	$x = 0.05$	$x = 0.10$	$x = 0.15$	$x = 0.20$	$x = 0.30$	$x = 0.40$
This work	900 °C	825 °C	775 °C	775 °C	725 °C	625 °C
Price et al.[22]	—	834 °C	—	738 °C	688 °C	602 °C

ΔS_{ox}^0 extracted from $\ln(K_{ox})$ vs. $1/T$ plots, at constant δ, for the different compositions La$_{1-x}$Ca$_x$FeO$_{3-\delta}$ are shown in Fig. 6c and d, respectively. Fig. 6c shows that for a given Ca dopant concentration x in the series La$_{1-x}$Ca$_x$FeO$_{3-\delta}$, ΔH_{ox}^0 becomes more exothermic with increasing δ, while at a fixed value of δ, ΔH_{ox}^0 becomes more endothermic (less exothermic) with increasing x.

The isotherms in Fig. 4 allow evaluation of the chemical potential of oxygen relative to that in equilibrium with gaseous O$_2$ at 1 atm,

$$\Delta\mu_O = \frac{RT}{2}\ln(pO_2) \tag{7}$$

The partial molar enthalpy of oxygen, Δh_O, and the partial molar entropy of oxygen, Δs_O, can be deduced from $\ln(pO_2)$ vs. $1/T$ (or equivalent) plots, at constant δ, according to

$$\ln(pO_2) = \frac{\Delta h_O}{2RT} - \frac{\Delta s_O}{2R} \tag{8}$$

Typical plots and resultant values of Δh_O and Δs_O for compositions La$_{1-x}$Ca$_x$FeO$_{3-\delta}$ are shown in Fig. S3.† In view of eqn (3), i.e., ignoring charge disproportionation (reaction (4)), the slopes of $\ln(K_{ox})$ vs. $1/T$ at constant δ relate to those derived from $\ln(pO_2)$ vs. $1/T$ plots. It follows

$$\Delta h_O = \frac{1}{2}\Delta H_{ox}^0\big|_\delta \tag{9}$$

The partial molar entropy can be represented as

$$\Delta s_O = \Delta s_O^0 - s_{conf} \tag{10}$$

where Δs_O^0 and s_{conf} are the non-configurational and configurational contributions, respectively. Analysis of the data of Δs_O obtained for the different compositions La$_{1-x}$Ca$_x$FeO$_{3-\delta}$, as shown in Fig. S3d,† indicates that significant departures occur from the ideal solution approximation, in which it is assumed that the configurational contribution to the entropy of the oxygen incorporation reaction (reaction (1)) is due to a random distribution of oxygen vacancies on the O sublattice and that of localized electron holes on the Fe sublattice. That is, the configurational contribution departs from the ideal form $s_{conf} = ((3 - \delta)/\delta) \times ((x - 2\delta)/(1 - (x - 2\delta)))^2$ (cf. eqn (2)). A more proper analysis awaits data of oxygen nonstoichiometry of compositions La$_{1-x}$Ca$_x$FeO$_{3-\delta}$ over more extended ranges in oxygen partial pressure and temperature than investigated in this study.

Regarded in terms of the reverse of reaction (1), i.e., the oxygen reduction reaction, the present results show that the energetic cost of formation of oxygen vacancies in La$_{1-x}$Ca$_x$FeO$_{3-\delta}$ is higher at higher oxygen nonstoichiometry, while smaller, at fixed δ, if La is partly substituted by Ca. These observations may be related, e.g., to an increase in the oxygen bond strength with increasing oxygen nonstoichiometry (due to the concomitant increase in the average oxidation state of the transition metal cation), a decrease in the oxygen bond strength with Ca content (Ca–O bonds are weaker than La–O bonds) and/or changes in the electronic structure. First principle calculations indeed confirm that the oxygen vacancy formation energy, $\Delta h_V (= -\Delta h_O = -1/2\Delta H_{ox}^0)$ is significantly lowered with alkaline–earth metal dopant concentrations in La$_{1-x}$Sr$_x$FeO$_{3-\delta}$ (ref. 28) and La$_{1-x}$Ca$_x$FeO$_{3-\delta}$ (ref. 29) which is in line with the results shown in Fig. 6c. Both cited studies show that the electron holes induced by Sr or Ca substitution have significant O 2p character as has been confirmed by experimental studies using X-ray absorption spectroscopy.[30] These findings suggest that the electron holes in both series of oxides are (at least, to some extent) delocalized due to which the mass action law is expected to break down.[31] Nonideal thermodynamic behavior of the defects as observed for La$_{1-x}$Ca$_x$FeO$_{3-\delta}$ in this study has also been reported for a number of related perovskite oxides, including Ba$_{1-x}$Sr$_x$FeO$_{3-\delta}$ ($x = 0$, 0.5),[32,33] (Ba$_{0.5}$Sr$_{0.5}$)$_{1.04}$Co$_{0.8}$Fe$_{0.2}$O$_{3-\delta}$,[32] Ba$_{0.5}$Sr$_{0.5}$Co$_{0.4}$Fe$_{0.6}$O$_{3-\delta}$,[32] La$_{0.4}$Sr$_{0.6}$Co$_{1-y}$Fe$_y$O$_{3-\delta}$ ($y = 0.2$, 0.4),[34] SrCo$_{0.8}$Fe$_{0.2}$O$_{3-\delta}$,[35] and La$_{1-x}$Sr$_x$CoO$_{3-\delta}$ ($0.1 \leq x \leq 0.7$).[31,36] These and present findings are, however, in contrast with data of high-temperature drop calorimetry and thermogravimetry on La$_{1-x}$Sr$_x$FeO$_{3-\delta}$.[17,18,37] In these studies, ΔH_{ox}^0 for La$_{1-x}$Sr$_x$FeO$_{3-\delta}$ is found virtually independent of the oxygen nonstoichiometry at an average value of -200 ± 50 kJ mol^{-1} for $0 \leq x \leq 0.5$ and at -140 ± 30 kJ mol^{-1} for $0.5 \leq x \leq 1.0$. Corresponding changes with x within the specified ranges are found to be within experimental error. Further work is required to understand the nonideal energetics of the defect species in La$_{1-x}$Ca$_x$FeO$_{3-\delta}$.

3.3 Electrical conductivity

Fig. 7a shows Arrhenius plots of the total electrical conductivity in air of the different compositions La$_{1-x}$Ca$_x$FeO$_{3-\delta}$. The conductivity includes both ionic and electronic contributions. Since under the given experimental conditions electron holes are the predominant charge carriers (Fig. 5) and their mobility will be much higher than that of oxygen vacancies, it can safely be assumed that the contribution of ionic conductivity to the total electrical conductivity is negligible.

Previous studies have suggested that electrical conduction in La$_{1-x}$A$_x$FeO$_3$ (A = Ca, Sr) at elevated temperatures occurs by p-type small polaron hopping,[16,20,38] and can be expressed as

$$\sigma_{el} = p\left(\frac{N_A}{V_m}\right)e\mu_h \tag{11}$$

This journal is © The Royal Society of Chemistry 2021

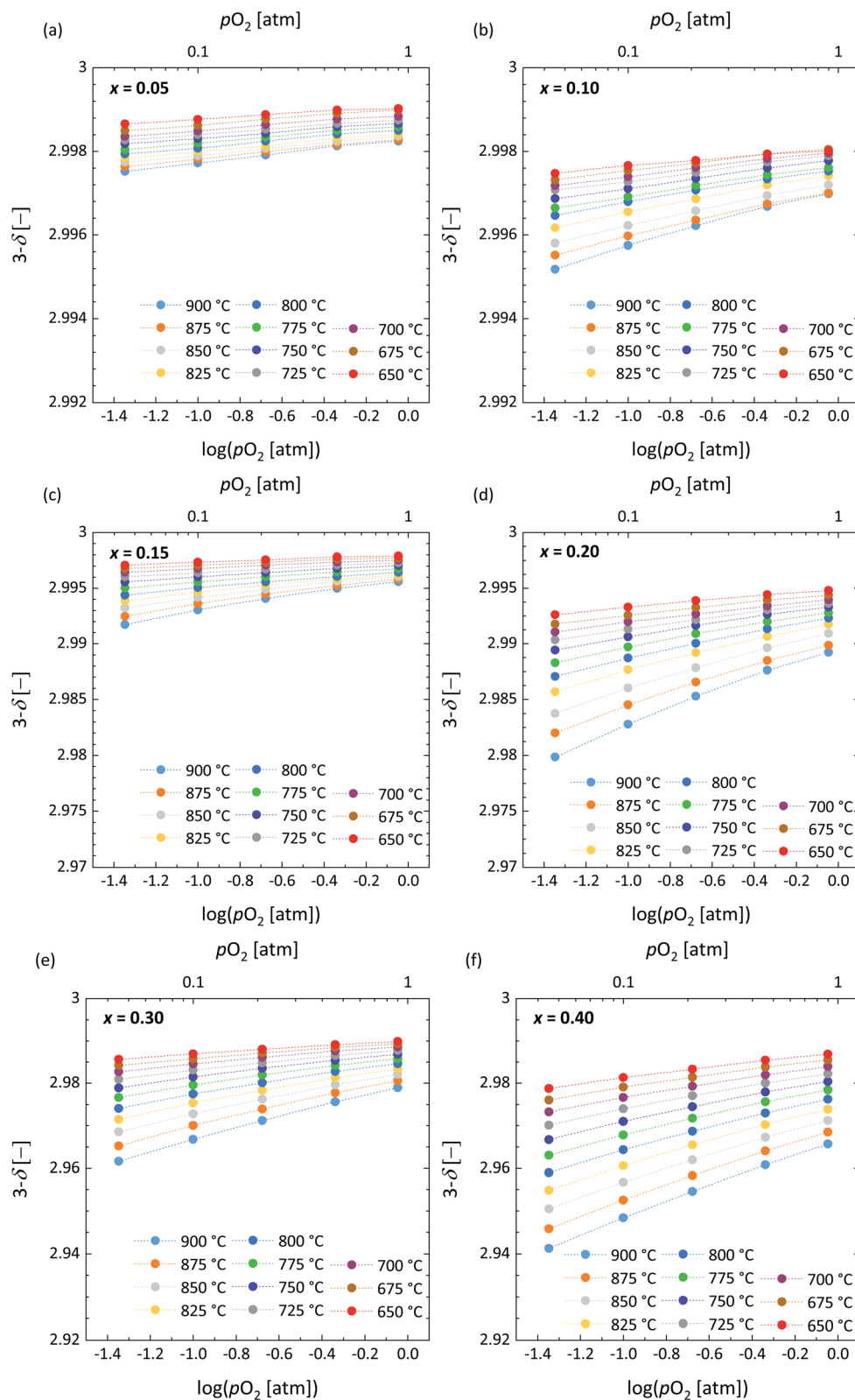J. Mater. Chem. A, 2021, **9**, 974–989 | **979**

Fig. 4 Oxygen stoichiometry $(3 - \delta)$ of $La_{1-x}Ca_xFeO_{3-\delta}$ for (a) $x = 0.05$, (b) $x = 0.10$, (c) $x = 0.15$, (d) $x = 0.20$, (e) $x = 0.30$ and (f) $x = 0.40$ as a function of $\log(pO_2)$ at different temperatures. Dashed lines are drawn to guide the eye. Data for $x = 0.40$ were taken from our previous study.[15]

where $p \equiv [Fe^{\bullet}_{Fe}]$ and μ_h are the concentration (mole fraction) and mobility of electron holes, respectively, is Avogadro's number, V_m is the molar volume, and e is the electronic charge.

The charge carrier concentration p as a function of temperature for each composition $La_{1-x}Ca_xFeO_{3-\delta}$ was determined from corresponding data of oxygen nonstoichiometry, while the
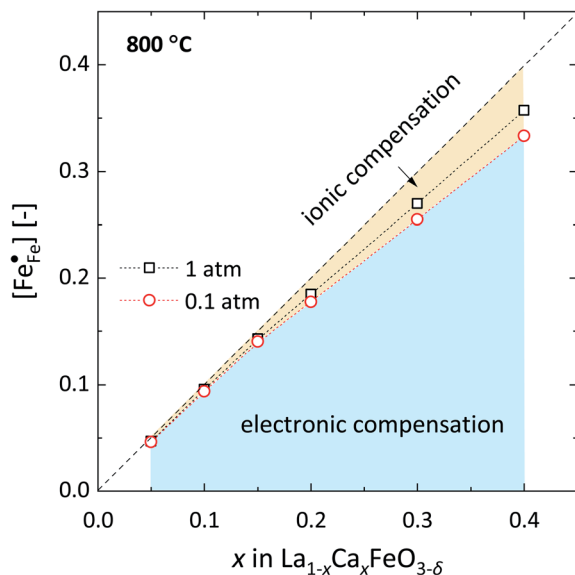
980 | *J. Mater. Chem. A*, 2021, **9**, 974–989

This journal is © The Royal Society of Chemistry 2021

Fig. 5 Electron hole concentration ($[Fe^{\bullet}_{Fe}]$) in $La_{1-x}Ca_xFeO_{3-\delta}$ as a function of x, at 800 °C, at $pO_2 = 0.1$ atm and $pO_2 = 1$ atm. The dotted lines are drawn to guide the eye. The dashed line denotes the limiting case of electronic compensation of the Ca dopant. The blue and beige areas represent an artistic view of the degrees of electronic and ionic compensation, at $pO_2 = 0.1$ atm. Note that the degree of electronic compensation increases at the expense of ionic compensation upon increasing the pO_2 from 0.1 atm to 1 atm.

mobility μ_h was calculated with the help of eqn (11). Arrhenius plots of both parameters for the different compositions $La_{1-x}Ca_xFeO_{3-\delta}$ are shown in Fig. 7b and c, respectively. Fig. 7a shows that the electrical conductivity of $La_{1-x}Ca_xFeO_{3-\delta}$, at 650 °C, increases with Ca mole fraction up to a value of 123 S cm^{-1} for $x = 0.3$. The results displayed in Fig. 7b make clear that this increase can be attributed to the concomitant increase in the charge carrier concentration. The lowering of electrical conductivity on going from composition $x = 0.3$ to $x = 0.4$ (Fig. 7a) is caused by the decreasing mobility, which is found much lower for $x = 0.40$ than for $x = 0.30$. The observed decrease of the electrical conductivity with temperature for both compositions $x = 0.30$ and $x = 0.40$ (Fig. 7a) can be attributed to a lowering of both the concentration and mobility of the charge carriers with increasing temperature.

To discriminate between adiabatic and non-adiabatic regimes of small polaron hopping, we have analyzed the electrical mobility in terms of Emin–Holstein's theory.[39–41] In the event of coincidence of local distortions of initial and final states, the temperature-dependent mobility in this theory is given by

$$\mu_h = \left(1 - [Fe^{\bullet}_{Fe}]\right) \frac{3}{2} \frac{ea^2 \nu_0}{k_B} \frac{1}{T} \exp\left(-\frac{\frac{1}{2}W_p - J}{k_B T}\right) \quad (12)$$

where a is the hopping distance, ν_0 is the frequency of optical phonons, W_p is the polaron binding energy, J is the kinetic energy of the polaron, and k_B is Boltzmann's constant. The factor of 3/2 takes into account the fact that the polaron moves
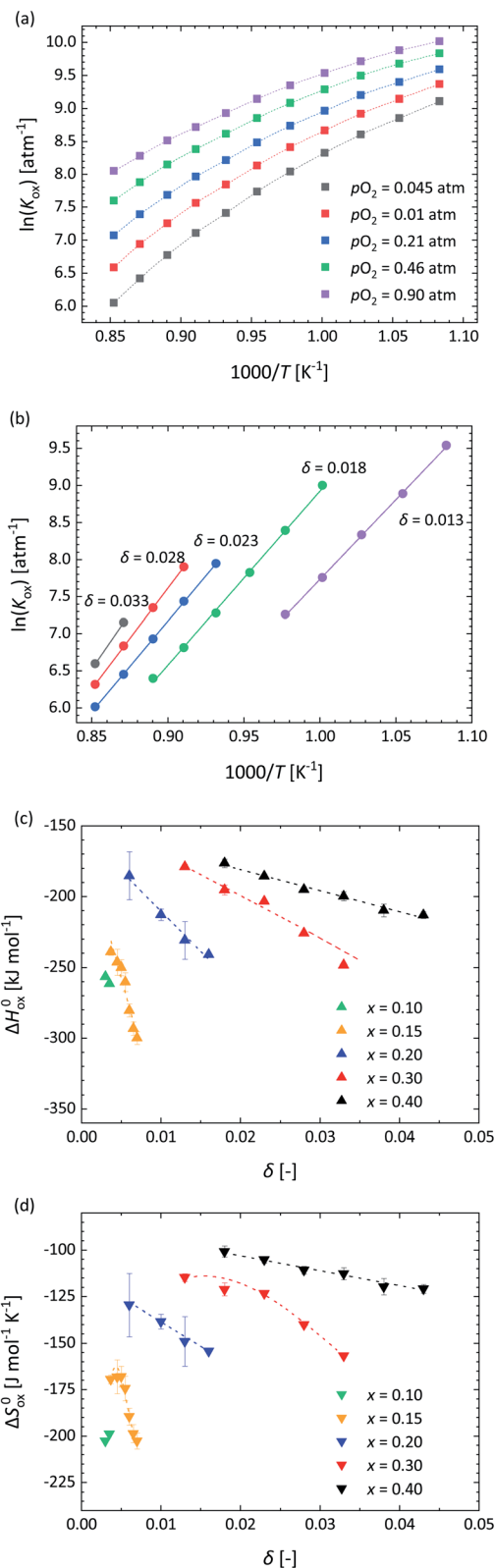

Fig. 6 van 't Hoff plots of K_{ox} for $La_{0.7}Ca_{0.3}FeO_{3-\delta}$ at (a) constant pO_2 and (b) constant δ. (c) Enthalpy (ΔH^0_{ox}) and (d) entropy (ΔS^0_{ox}) of oxidation (reaction (1)) at given values of x in $La_{1-x}Ca_xFeO_{3-\delta}$ as a function of δ. Data in (c) and (d) were extracted from $\ln(K_{ox})$ vs. $1/T$ plots, at constant δ.
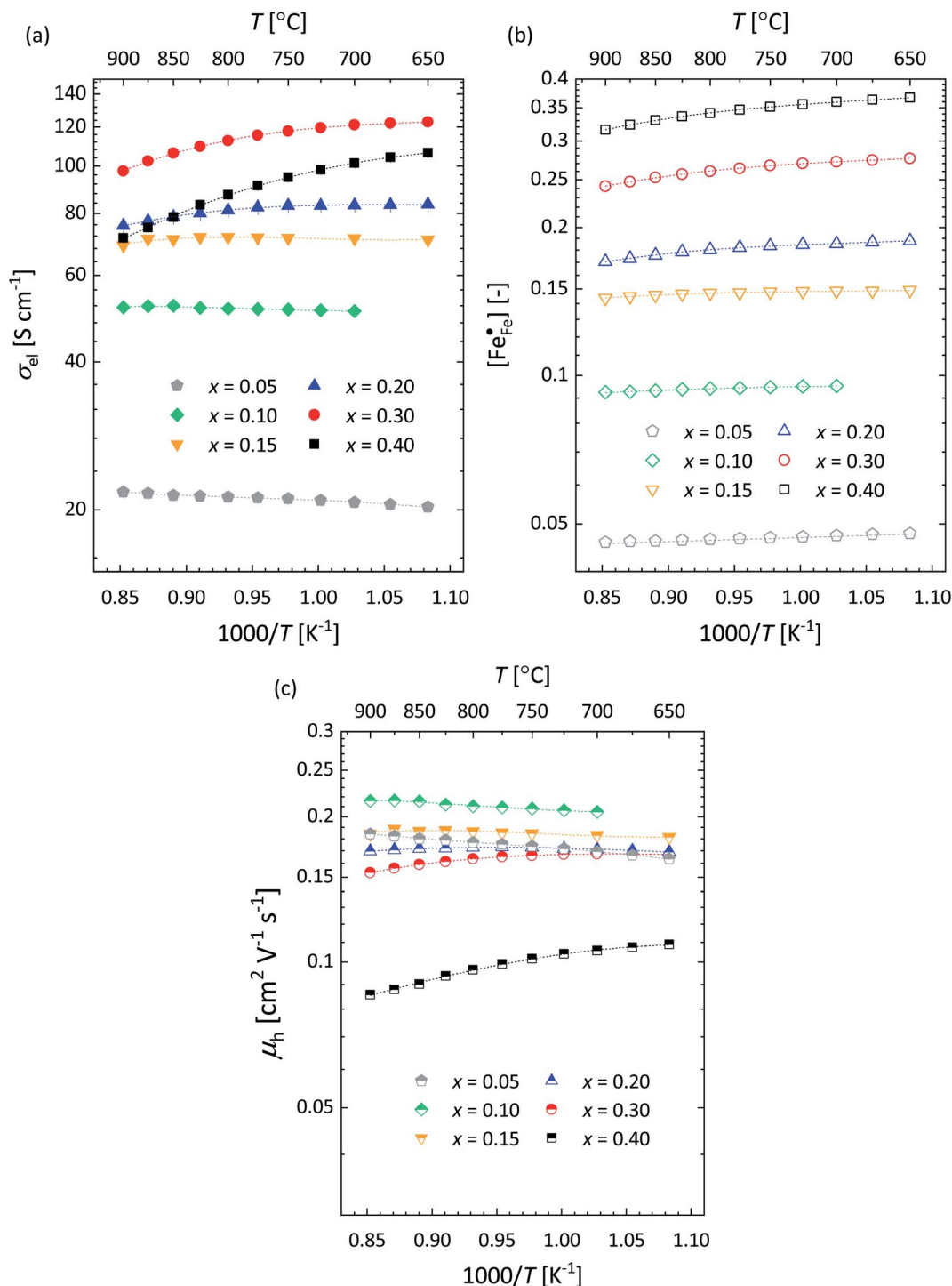
Fig. 7 Arrhenius plots of the (a) electrical conductivity (σ_{el}), (b) concentration of electron holes ($[Fe_{Fe}^{\bullet}]$) and (c) mobility of electron holes (μ_h) for $La_{1-x}Ca_xFeO_{3-\delta}$, at $pO_2 = 0.21$ atm. The dashed lines are drawn to guide the eye.

in a three-dimensional lattice.[41] The factor of $(1 - [Fe_{Fe}^{\bullet}])$ takes into account the probability that the adjacent site to which the polaron hops may already be occupied.[42] Accordingly, the plot of $\ln\{\mu_h T/(1 - [Fe_{Fe}^{\bullet}])\}$ vs. $1000/T$ should give a straight line with activation energy $E_a = \frac{1}{2}W_p - J$ in the adiabatic regime. In the non-adiabatic regime,[39] the charge carrier moves too slowly to adjust to rapid lattice fluctuations and, hence, misses such

'coincidence events', lowering the net hopping rate. The mobility of electron holes is then given by

$$\mu_h = (1 - [Fe_{Fe}^{\bullet}]) \frac{3}{2} \frac{ea^2\nu_0}{k_B} \frac{\pi J^2}{h} \left(\frac{2\pi}{W_p k_B}\right)^{1/2} \frac{1}{T^{3/2}} \exp\left(-\frac{\frac{1}{2}W_p}{k_B T}\right)$$
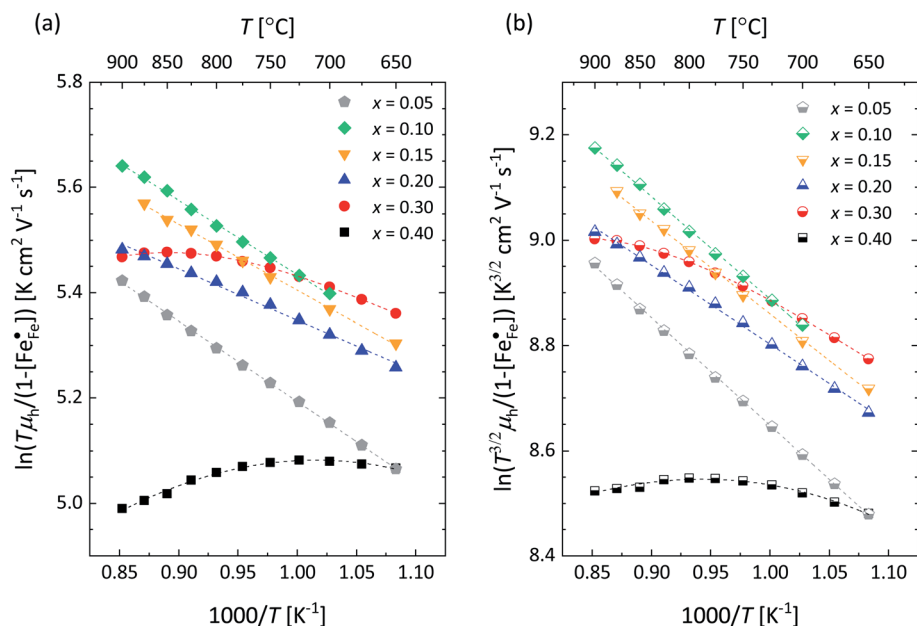
(13)

Fig. 8 Plots of (a) $\ln\{\mu_h T/(1 - [Fe_{Fe}^{\bullet}])\}$ vs. $1000/T$ (adiabatic regime) and (b) $\ln\{\mu_h T^{3/2}/(1 - [Fe_{Fe}^{\bullet}])\}$ vs. $1000/T$ (non-adiabatic regime) for $La_{1-x}Ca_xFeO_{3-\delta}$ at $pO_2 = 0.21$ atm. The dashed lines are drawn to guide the eye.

where h is Planck's constant. In this case, the plot of $\ln\{\mu_h T^{3/2}/(1 - [Fe_{Fe}^{\bullet}])\}$ vs. $1000/T$ should give a straight line with activation energy $E_a = \frac{1}{2}W_p$. Fig. 8a and b show corresponding data fitted to each model. The equations for the linear relationships along with the coefficients of determination (R^2) are presented in Table 3. Both models fit the data for compositions $x = 0.05, 0.10, 0.15$ and 0.20 reasonably well. Based on the results, however, it is difficult to substantiate either model. Comparison of the obtained R^2 values indicates a slight favor for the non-adiabatic model. Clear departures from linear relationships are, however, obtained for compositions $x = 0.30$ and 0.40.

Fig. S4a† shows the pO_2 dependence of the electrical conductivity of $La_{1-x}Ca_xFeO_{3-\delta}$, at 800 °C. For all compositions, it is found that the calculated electron hole mobility is suppressed by decreasing pO_2, suggesting that the presence of oxygen vacancies highly influences the apparent mobility, e.g., by disruption of Fe^{4+}–O–Fe^{3+} migration pathways, oxygen vacancies acting as traps or as scattering centres for the electrons (Fig. S4b and S5†).

Above, we have analyzed the apparent hole mobility in $La_{1-x}Ca_xFeO_{3-\delta}$ in terms of hopping of small polarons, which is

a thermally activated process. As seen from Fig. 7c, the apparent hole mobility in the compositions with $x = 0.30$ and 0.40 is rather found to decrease with increasing temperature. As alluded to before, several studies based on density functional theory and X-ray adsorption spectroscopy have revealed that the Fe 3d and O 2p states in $La_{1-x}A_xFeO_{3-\delta}$ (A = Ca, Sr) and related perovskites are hybridized to some degree. The extent of hybridisation is proposed to increase with the oxidation state of the transition metal ion,[43] causing increased delocalisation of the charge carriers. Clearly, more research is warranted to clarify the nature of the charge carriers in these solids.

3.4 Electrical conductivity relaxation

The oxygen transport properties of phases $La_{1-x}Ca_xFeO_{3-\delta}$ were evaluated using the ECR technique. It is recalled that measurements were conducted using small pO_2 steps, i.e., between 0.100 and 0.215 atm, ensuring conditions close to equilibrium. Fig. 9 shows normalized conductivity relaxation curves for a given sample obtained for oxidation steps at different temperatures along with the respective fits to the theoretical model. It can be seen that the time needed to reach equilibrium is longer as the temperature is reduced. Curve

Table 3 Linear equations used to fit $\ln\{\mu_h T/(1 - [Fe_{Fe}^{\bullet}])\}$ vs. $1000/T$ (adiabatic regime) and $\ln\{\mu_h T^{3/2}/(1 - [Fe_{Fe}^{\bullet}])\}$ vs. $1000/T$ (non-adiabatic regime) plots as shown in Fig. 8a and b, respectively, along with the coefficients of determination (R^2)

	Adiabatic		Non-adiabatic	
	$\ln\{\mu_h T/(1 - [Fe_{Fe}^{\bullet}])\}$	R^2	$\ln\{\mu_h T^{3/2}/(1 - [Fe_{Fe}^{\bullet}])\}$	R^2
$x = 0.05$	$-1526.50/T + 6.72$	0.99957	$-2045.87/T + 10.68$	0.99959
$x = 0.10$	$-1409.57/T + 6.84$	0.99884	$-1943.11/T + 10.82$	0.99917
$x = 0.15$	$-1253.09/T + 6.65$	0.99881	$-1766.98/T + 10.64$	0.99907
$x = 0.20$	$-977.47/T + 6.33$	0.99333	$-1496.84/T + 10.29$	0.99821

This journal is © The Royal Society of Chemistry 2021
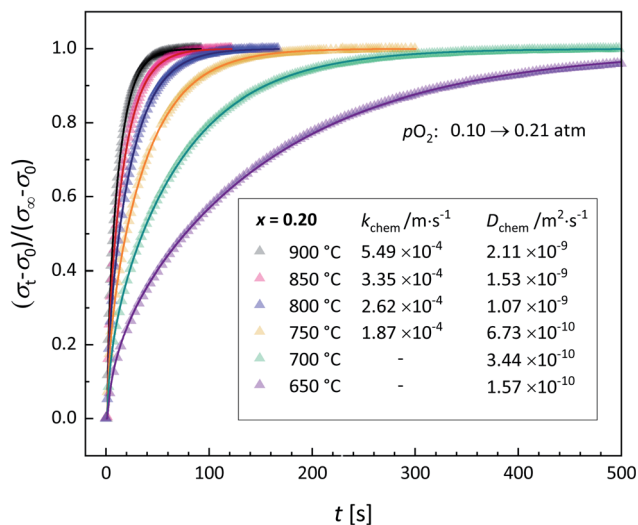
J. Mater. Chem. A, 2021, **9**, 974–989 | **983**

Fig. 9 Typical normalized conductivity curves following a step change in pO_2 from 0.100 to 0.215 atm at different temperatures. Data shown were obtained for $La_{0.8}Ca_{0.2}FeO_{3-\delta}$. The solid lines show the least-square fitting to the model equations. Corresponding values of D_{chem} and k_{chem} obtained from fitting are listed.

fitting allows simultaneous determination of the chemical diffusion coefficient, D_{chem}, and the surface exchange coefficient, k_{chem}, provided that fitting is sensitive to both parameters. Both parameters can be most reliably assessed from fitting if the sample length is close to D_{chem}/k_{chem}, as parameterized by the Biot number (Bi).[44] This number represents the ratio between the characteristic times for diffusion, $\tau_{diff} = l_z^2/D_{chem}$, and that for surface exchange, $\tau_{exch} = l_z/k_{chem}$, l_z being the half-thickness of the sample,

$$\text{Bi} = \frac{\tau_{exch}}{\tau_{diff}} = \frac{l_z}{D_{chem}/k_{chem}} \quad (14)$$

D_{chem} and k_{chem} can be most reliably assessed in the 'mixed-controlled' region. This confidence region is, however, determined by the accuracy of the measurements. A plot of the Biot number against temperature obtained from fitting of the conductivity relaxation curves as acquired for the series of $La_{1-x}Ca_xFeO_{3-\delta}$ is shown in Fig. 10. Note from eqn (14) that the Biot number can only be calculated if both D_{chem} and k_{chem} are obtained from curve fitting.

Arrhenius plots of D_{chem} and k_{chem} for the different $La_{1-x}Ca_xFeO_{3-\delta}$ compositions are shown in Fig. 11a and b, respectively. There is no significant difference between the results from oxidation and reductions runs. Obtained values of D_{chem} for $x = 0.10$ and $x = 0.20$ are in good agreement with corresponding values reported by Berger et al.[12,23] (Fig. 11a). The agreement is less good comparing values of k_{chem} for $x = 0.20$ with those reported by Berger et al.[12] (Fig. 11b). This may at least partly be due to the difficulty in determining k_{chem} as the materials exhibit exceptionally high surface exchange rates, as was noted before by Berger et al.[23] In the present study, values of k_{chem} could only be accurately assessed from the relaxation curves for compositions $x = 0.15$, $x = 0.20$, $x = 0.30$ and $x = 0.40$. Note from Fig. 11b that all these compositions show
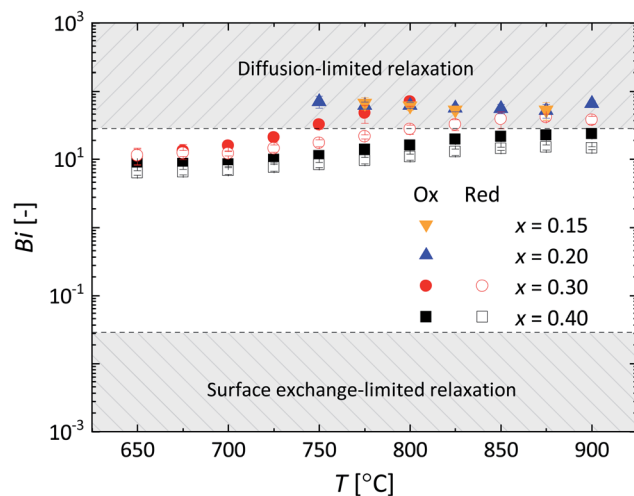

Fig. 10 Temperature dependence of the Biot number (Bi) for $La_{1-x}Ca_xFeO_{3-\delta}$. Error bars are within the size of the symbols. Following Den Otter et al.[25] the mixed-controlled region is found for $0.03 \leq Bi \leq 30$.

higher surface exchange rates than state-of-the-art $La_{0.58}Sr_{0.4}Co_{0.2}Fe_{0.8}O_{3-\delta}$ (LSCF).[45] Recent research has learned that the surface exchange rate on oxide surfaces may be highly influenced by, e.g., surface enrichment due to segregation, surface impurities and grain size.[5,6,45] The high exchange rates found for $La_{1-x}Ca_xFeO_{3-\delta}$ deserve more focused research, but this is considered beyond the scope of this work.

Apart from $x = 0.05$, the temperature dependences of D_{chem} of compositions $La_{1-x}Ca_xFeO_{3-\delta}$ exhibit non-Arrhenius behavior (Fig. 11a). The variation in slope with temperature is linked with the existence regions of the orthorhombic (space group $Pbnm$) and rhombohedral (space group $R\bar{3}c$) phases as may be inferred by comparing the data in Fig. 11a with the structural data shown in Fig. 3. Apparent activation energies of D_{chem} in both temperature regions deduced from the data in Fig. 11a are listed in Table S2.† Note from this table that significantly higher activation energies are found in the temperature region of the orthorhombic phase. As D_{chem} is a lumped parameter, the different activation energies in both temperature regions may either have a kinetic or a thermodynamic origin.

3.5 Ionic conductivity and oxygen diffusivity

To further analyze the influence of Ca substitution on the oxygen transport properties of $La_{1-x}Ca_xFeO_{3-\delta}$, the oxygen self-diffusion coefficient, D_s, and vacancy diffusion coefficient, D_v, of the different compositions were calculated. D_s was calculated, using the relationship[19]

$$D_{chem} = \gamma_O D_s \quad (15)$$

where γ_O is the thermodynamic factor, defined as

$$\gamma_O = \frac{1}{2} \times \frac{\partial \ln(pO_2)}{\partial \ln(c_O)} = \frac{3-\delta}{2} \times \frac{\partial \ln(pO_2)}{\partial(3-\delta)} \quad (16)$$

and where $c_O(= (3-\delta)/V_m)$ is the oxygen concentration, while D_v was calculated within the random walk diffusion theory framework, using the jump balance,[46]
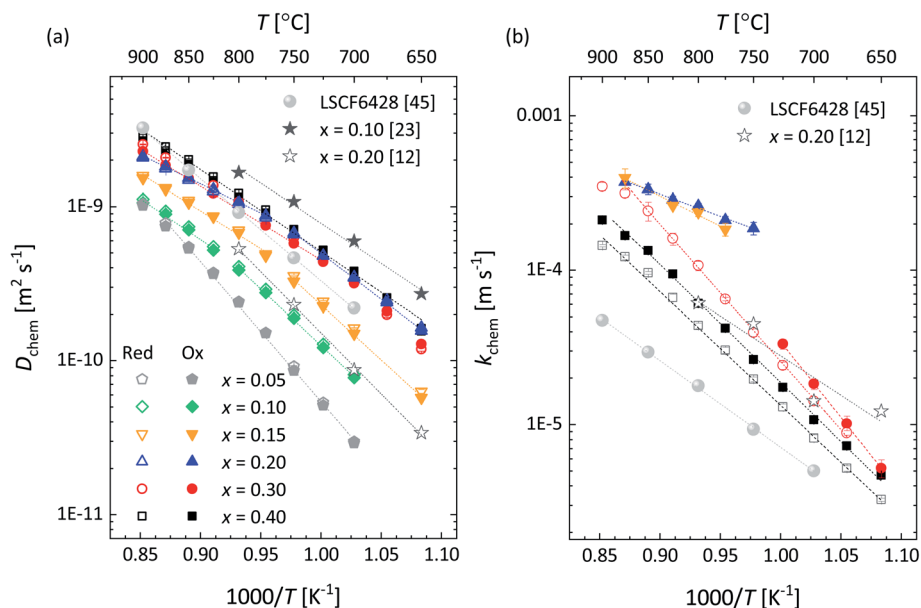
984 | J. Mater. Chem. A, 2021, 9, 974–989

This journal is © The Royal Society of Chemistry 2021

Fig. 11 Arrhenius plots of the (a) chemical diffusion coefficient (D_{chem}) and (b) surface exchange coefficient (k_{chem}) for $La_{1-x}Ca_xFeO_{3-\delta}$ (0.100 ↔ 0.215 atm). Filled and open symbols represent data of oxidation and reduction step changes, respectively (for data from this study only). Error bars are within the size of the symbols. The dashed lines are from linear fitting of the data. Data for $La_{0.9}Ca_{0.1}FeO_{3-\delta}$ (0.10 ↔ 0.15 atm),[22] $La_{0.8}Ca_{0.2}FeO_{3-\delta}$ (0.10 ↔ 0.15 atm),[12] and $La_{0.58}Sr_{0.4}Co_{0.2}Fe_{0.8}O_{3-\delta}$ (LSCF6428; 0.20 ↔ 0.40 atm)[43] from the cited literature are shown for comparison. The pressure range between brackets denotes the step change in pO_2 used in the ECR measurements.

$$c_O \times D_s = c_v \times D_v \tag{17}$$

where $c_v (= \delta/V_m)$ is the oxygen vacancy concentration. The temperature dependences of γ_O, at $pO_2 = 0.147$ atm, for the different compositions $La_{1-x}Ca_xFeO_{3-\delta}$ investigated in this work are given in Fig. S6,† noting that the specified pO_2 corresponds to the logarithmic average of the pO_2 step change (0.100

↔ 0.215 atm) used in the ECR experiments. Arrhenius plots of D_s and D_v are shown in Fig. 12a and b, respectively. Both plots are highly linear with coefficients of determination (R^2) close to unity, which confirms not only that the observed non-Arrhenius behavior of D_{chem} (see previous section) has a sole thermodynamic origin, but also that the orthorhombic-to-rhombohedral phase transition has negligible influence on the diffusivity of
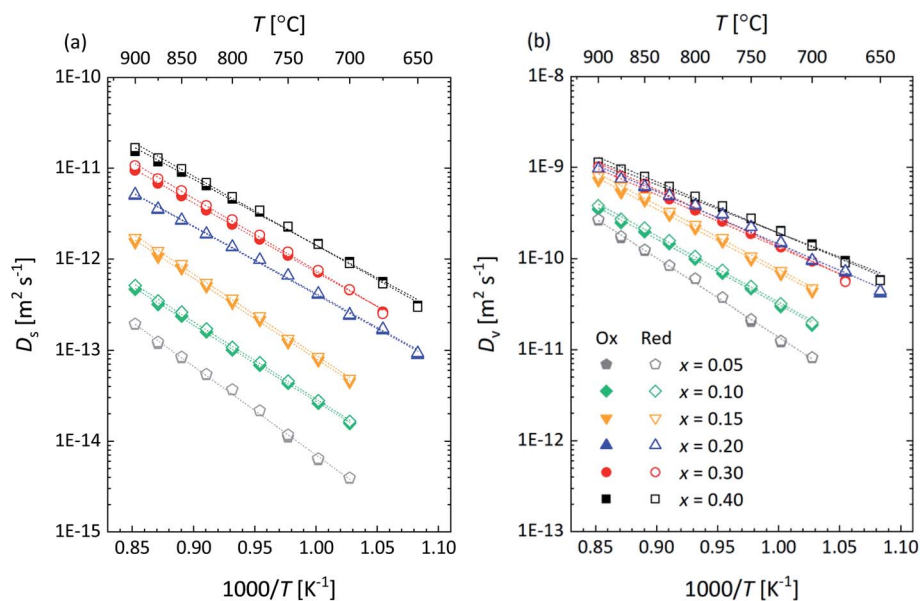

Fig. 12 Arrhenius plots of the (a) oxygen self-diffusion coefficient (D_s) and (b) oxygen vacancy diffusion coefficient (D_v) for $La_{1-x}Ca_xFeO_{3-\delta}$, at $pO_2 = 0.147$ atm. The filled and open symbols represent the data of oxidation and reduction step changes, respectively. Error bars are within the size of the symbols. The drawn lines are from linear fitting of the data. The specified pO_2 corresponds to the logarithmic average of the step change in pO_2 (0.100 ↔ 0.215 atm) used in the ECR measurements.

This journal is © The Royal Society of Chemistry 2021

J. Mater. Chem. A, 2021, **9**, 974–989 | **985**

oxygen in $La_{1-x}Ca_xFeO_{3-\delta}$. Calculated activation energies of D_s and D_v are listed in Tables S3 and S4,† respectively. For both parameters, good agreement is noted between the values deduced from data of oxidation and reductions runs. Values of D_v for $La_{1-x}Ca_xFeO_{3-\delta}$ from this study are compared with literature data for $La_{1-x}Ca_xFeO_{3-\delta}$ ($x = 0.1, 0.2$),[12,23] $La_{1-x}Sr_x$-$FeO_{3-\delta}$ ($x = 0.1, 0.25, 0.5$),[47,48] $La_{1-x}Sr_xCoO_{3-\delta}$ ($x = 0.2, 0.5$)[49] and $La_{0.6}Sr_{0.4}Co_{0.2}Fe_{0.8}O_{3-\delta}$ (ref. 50) in Fig. S7.† This comparison shows that the differences in the values of D_v are relatively small, reinforcing the concept that in order to have high ionic conductivities in these perovskite-structured materials, the oxygen vacancy concentration must be high, as has been recognized previously by Mizusaki[51] and Kilner.[52]

Fig. 13 shows Arrhenius plots of the ionic conductivity, σ_{ion}, of $La_{1-x}Ca_xFeO_{3-\delta}$ calculated using the Nernst–Einstein equation,

$$\sigma_{ion} = \frac{4e^2 N_A c_O\ D_s}{k_B T} = \frac{4e^2 N_A c_v D_v}{k_B T} \quad (18)$$

The obtained results clearly reveal that the isothermal value of σ_{ion} increases with the mole fraction x of the Ca dopant. This is due to the increase in the concentration of oxygen vacancies with x in $La_{1-x}Ca_xFeO_{3-\delta}$ as can be inferred from the data presented in Fig. 4, but at least in part due to the concomitant increase in D_v as is shown in Fig. 14a. The results in the latter figure demonstrate that D_v at fixed temperature increases with
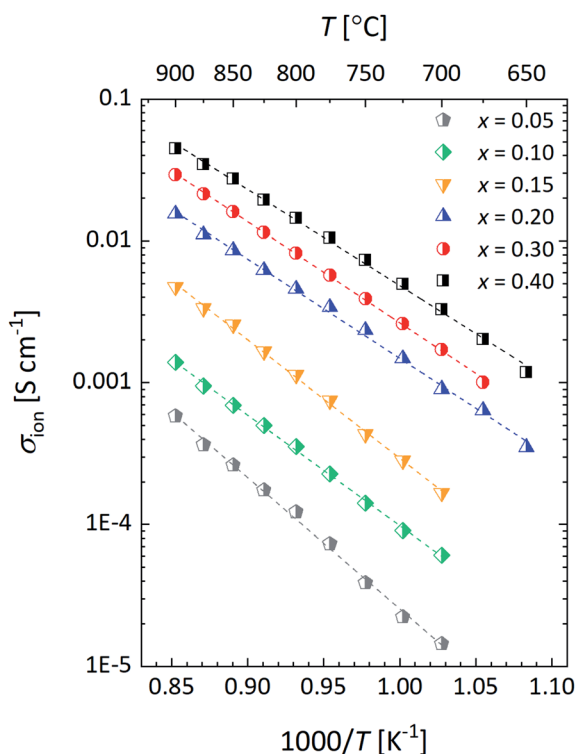

(a)

(b)

Fig. 14 (a) Oxygen vacancy diffusion coefficient (D_v) and (b) migration energy (E_m) as a function of x in $La_{1-x}Ca_xFeO_{3-\delta}$ as derived from data presented in Fig. 12b.

Ca content to reach an almost constant value at $x \geq 0.20$. The observed behavior is consistent with the concomitant decrease in the oxygen migration barrier, E_m, with increasing x in $La_{1-x}Ca_xFeO_{3-\delta}$ as shown in Fig. 14b. E_m is found to decrease from 1.72 ± 0.02 eV for $x = 0.05$ to an average value of 1.08 ± 0.03 eV for $x = 0.40$ (Table S4†). The observed migration barriers at small values of x are distinctly larger than those reported for single crystals of $La_{1-x}Sr_xCoO_{3-\delta}$ (77 ± 21 kJ mol^{-1} ($x = 0$), 79 ± 25 kJ mol^{-1} ($x = 0.1$))[47] and $La_{1-x}Sr_xFeO_{3-\delta}$ (74 ± 24 kJ mol^{-1} ($x = 0$), 79 ± 25 kJ mol^{-1} ($x = 0.1$), 114 ± 23 kJ mol^{-1} ($x = 0.25$) by Ishigaki et al.[47]

The motion of oxygen ions through the oxide lattice is described by an activated hopping process and involves the

Fig. 13 Arrhenius plots of the calculated ionic conductivity (σ_{ion}) for $La_{1-x}Ca_xFeO_{3-\delta}$, at $pO_2 = 0.147$ atm. Lines are drawn to guide the eye. The specified pO_2 corresponds to the logarithmic average of the step change in pO_2 (0.100 ↔ 0.215 atm) used in the ECR measurements.

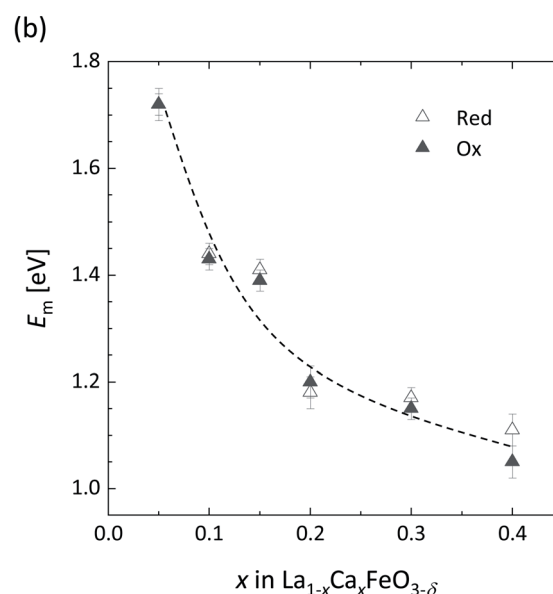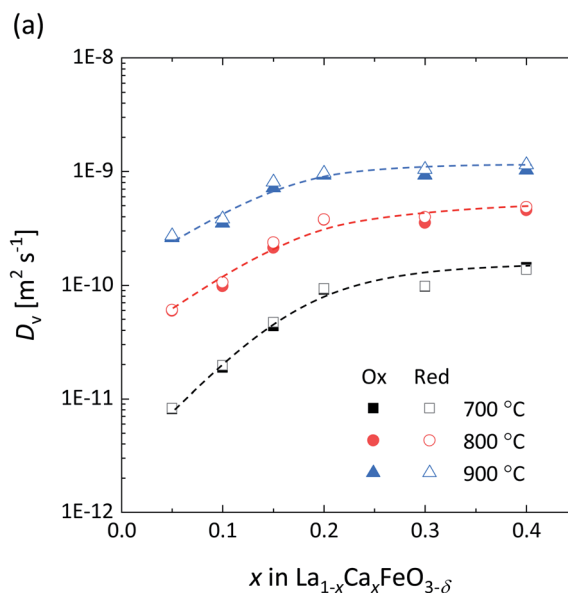986 | J. Mater. Chem. A, 2021, 9, 974–989

This journal is © The Royal Society of Chemistry 2021

breaking of cations bonds with oxygen and partial charge transfer from oxygen to the adjacent transition metal or the Fermi level (*i.e.*, resembling the process of oxygen vacancy formation) and migration along the minimum energy pathway to the next nearest-neighbor site, thereby migrating through a critical A_2B triangle (formed by two A cations and one B cation). Many researchers have attempted to correlate the experimentally observed migration barriers with various descriptors, like the free lattice volume, oxygen bond strength, lattice distortion, critical radius, *etc.*[53-56] Using *ab initio* methods, Mayeshiba and Morgan[57] found that descriptors like the O p-band center energy and oxygen vacancy formation energy correlate well with the oxygen migration barrier for a group of over 40 perovskite oxides. Both descriptors are related to the metal–oxygen bond strength, which obviously raises the question whether one of the used descriptors is redundant. The O p-band center energy (which is defined as the centroid of the projected density of states (PDOS) relative to the Fermi level) is found to correlate well with the oxygen vacancy formation enthalpy, which suggests that electronic contributions are highly important to oxygen vacancy formation in perovskite oxides.[57-60]

Assuming that all oxygen sites are equivalent, random walk theory of diffusion predicts that the vacancy diffusivity D_v is directly proportional to the fraction of occupied sites and, hence, to the oxygen concentration c_O which, for small values of the oxygen vacancy concentration c_v, is virtually constant.[61] For this reason, measured activation energies of D_v are commonly interpreted as the migration energy (E_m), assuming that all other atomistic parameters, including the characteristic lattice frequency and hopping distance, remain constant with changes in c_v. Fig. 15 shows the migration barriers thus obtained for $La_{1-x}Ca_xFeO_{3-\delta}$ (Table S4†).

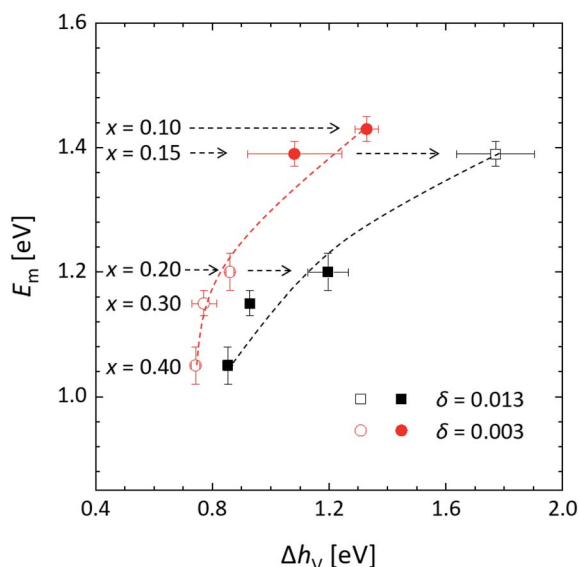plotted against the oxygen vacancy formation energies, Δh_V, at two different values of δ, as evaluated from corresponding van 't Hoff plots (Fig. 6b). Both curves exhibit a trend similar to that observed for the group of perovskite oxides by Mayeshiba and Morgan[57] in the sense that the migration barrier in $La_{1-x}Ca_xFeO_{3-\delta}$ is found to decrease with decreasing Δh_V. As discussed in Section 3.2, values of Δh_V for $La_{1-x}Ca_xFeO_{3-\delta}$ depend both on x and δ. A more detailed analysis of the correlation between E_m and Δh_V in $La_{1-x}Ca_xFeO_{3-\delta}$ must therefore await evaluation of the migration barriers in compositions $La_{1-x}Ca_xFeO_{3-\delta}$ as a function of both x and δ.

4. Conclusions

In this work, we have shown that:

(i) Perovskite-type oxides $La_{1-x}Ca_xFeO_{3-\delta}$ ($x = 0.05, 0.10, 0.15, 0.20, 0.30$ and 0.40) exhibit a phase transition, under ambient air, from room-temperature orthorhombic (space group $Pbnm$) to a rhombohedral (space group $R\bar{3}c$), *i.e.*, a slightly distorted cubic, structure at elevated temperature. The transition temperature decreases gradually from 900 °C for $x = 0.05$ to 625 °C for $x = 0.40$.

The combined data of thermogravimetry, electrical conductivity and electrical conductivity relaxation measurements on $La_{1-x}Ca_xFeO_{3-\delta}$ reveal that:

(ii) the Ca dopant is predominantly compensated by the formation of electron holes (electronic compensation) rather than by oxygen vacancies (ionic compensation). The enthalpy of oxidation is found to decrease with increasing oxygen non-stoichiometry δ, while it becomes more endothermic (less exothermic), at constant δ, with increasing x.

(iii) Maximum electrical conductivity of value 123 S cm^{-1} at 650 °C is found, under air, for $x = 0.30$. The temperature dependence of the calculated mobility of electron holes $x = 0.10, 0.15, 0.15$ and 0.20 is found to be in accordance with Emin–Holstein's theory (adiabatic and non-adiabatic regimes), but fails for the compositions with high Ca contents $x = 0.30$ and $x = 0.40$. This is tentatively explained by the increased delocalization of charge carriers with increasing the Ca dopant concentration.

(iv) The effective migration barrier for oxygen diffusion in $La_{1-x}Ca_xFeO_{3-\delta}$ decreases with decreasing oxygen vacancy formation enthalpy (less negative enthalpy of oxidation). The latter is found to depend both on Ca content and the level of oxygen nonstoichiometry. The ionic conductivity increases with increasing Ca content in $La_{1-x}Ca_xFeO_{3-\delta}$ due to the resultant increases in oxygen nonstoichiometry and vacancy diffusivity.

Conflicts of interest

There are no conflicts to declare.

Fig. 15 Migration energy (E_m) *vs.* oxygen vacancy formation energy (Δh_V). E_m was evaluated at constant pO_2 (extracted from data presented in Fig. 12b), while $\Delta h_V = -1/2\Delta H_{ox}^0$ was evaluated at constant oxygen nonstoichiometry (extracted from data presented in Fig. 6c), at $\delta = 0.003$ and at $\delta = 0.013$. Data presented by open symbols were obtained by extrapolation.

This journal is © The Royal Society of Chemistry 2021

J. Mater. Chem. A, 2021, **9**, 974–989 | **987**

References

1 S. Y. Gómez and D. Hotza, *Renewable Sustainable Energy Rev.*, 2016, **61**, 155–174.

2 J. C. Ruiz-Morales, D. Marrero-López, J. Canales-Vázquez and J. T. S. Irvine, *RSC Adv.*, 2011, **1**, 1403–1414.

3 C. Sun, R. Hui and J. Roller, *J. Solid State Electrochem.*, 2010, **14**, 1125–1144.

4 M. B. Mogensen, M. Chen, H. L. Frandsen, C. Graves, J. B. Hansen, K. V. Hansen, A. Hauch, T. Jacobsen, S. H. Jensen, T. L. Skafte and X. Sun, *Clean Energy*, 2019, **3**, 175–201.

5 J. Druce, H. Téllez, M. Burriel, M. D. Sharp, L. J. Fawcett, S. N. Cook, D. S. McPhail, T. Ishihara, H. H. Brongersma and J. a. Kilner, *Energy Environ. Sci.*, 2014, **7**, 3593–3599.

6 Đ. Tripković, R. Küngas, M. B. Mogensen and P. V. Hendriksen, *J. Mater. Chem. A*, 2019, **7**, 11782–11791.

7 W. Jung and H. L. Tuller, *Energy Environ. Sci.*, 2012, **5**, 5370–5378.

8 D. Oh, D. Gostovic and E. D. Wachsman, *J. Mater. Res.*, 2012, **27**, 1992–1999.

9 F. Morin, G. Trudel and Y. Denos, *Solid State Ionics*, 1997, **96**, 129–139.

10 J. Ovenstone, J. S. White and S. T. Misture, *J. Power Sources*, 2008, **181**, 56–61.

11 J. M. Ralph, C. Rossignol and R. Kumar, *J. Electrochem. Soc.*, 2003, **150**, 1518–1522.

12 C. Berger, E. Bucher, A. Windischbacher, A. D. Boese and W. Sitte, *J. Solid State Chem.*, 2018, **259**, 57–66.

13 C. Berger, E. Bucher, C. Gspan, A. Menzel and W. Sitte, *J. Electrochem. Soc.*, 2017, **164**, F3008–F3018.

14 B. C. H. Steele, K. M. Hori and S. Uchino, *Solid State Ionics*, 2000, **135**, 445–450.

15 J. Song, D. Ning and H. J. M. Bouwmeester, *Phys. Chem. Chem. Phys.*, 2020, **22**, 11984–11995.

16 J. Mizusaki, T. Sasamoto, W. R. Cannon and H. K. Bowen, *J. Am. Ceram. Soc.*, 1983, **66**, 247–252.

17 J. Mizusaki, M. Yoshihiro, S. Yamauchi and K. Fueki, *J. Solid State Chem.*, 1985, **58**, 257–266.

18 J. Mizusaki, M. Yoshihiro, S. Yamauchi and K. Fueki, *J. Solid State Chem.*, 1987, **67**, 1–8.

19 J. E. Ten Elshof, M. H. R. Lankhorst and H. J. M. Bouwmeester, *J. Electrochem. Soc.*, 1997, **144**, 1060–1067.

20 M. V. Patrakeev, I. A. Leonidov, V. L. Kozhevnikov and K. R. Poeppelmeier, *J. Solid State Chem.*, 2005, **178**, 921–927.

21 A. Fossdal, M. Menon, I. Waernhus, K. Wiik, M.-A. Einarsrud and T. Grande, *J. Am. Ceram. Soc.*, 2010, **87**, 1952–1958.

22 P. M. Price, E. Rabenberg, D. Thomsen, S. T. Misture and D. P. Butt, *J. Am. Ceram. Soc.*, 2014, **97**, 2241–2248.

23 C. Berger, E. Bucher and W. Sitte, *Solid State Ionics*, 2017, **299**, 46–54.

24 L. Winnubst, S. A. Veldhuis, R. Ruhl, S. F. P. ten Donkelaar, H. J. M. Bouwmeester and A. Nijmeijer, *Ceram. Int.*, 2015, **41**, 13709–13715.

25 J. Rodríguez-carvajal, *Phys. Rev. B: Condens. Matter Mater. Phys.*, 1993, **15**, 49–55.

26 M. W. den Otter, H. J. M. Bouwmeester, B. A. Boukamp and H. Verweij, *J. Electrochem. Soc.*, 2001, **148**, J1–J6.

27 R. D. Shannon, *Acta Crystallogr., Sect. A: Cryst. Phys., Diffr., Theor. Gen. Crystallogr.*, 1976, **32**, 751–767.

28 A. M. Ritzmann, A. B. Muñoz-García, M. Pavone, J. A. Keith and E. A. Carter, *Chem. Mater.*, 2013, **25**, 3011–3019.

29 R. Pushpa, D. Daniel and D. P. Butt, *Solid State Ionics*, 2013, **249–250**, 184–190.

30 M. Abbate, F. M. F. de Groot, J. C. Fuggle, A. Fujimori, O. Strebel, F. Lopez, M. Domke, G. Kaindl, G. A. Sawatzky, M. Takano, Y. Takeda, H. Eisaki and S. Uchida, *Phys. Rev. B: Condens. Matter Mater. Phys.*, 1992, **46**, 4511–4519.

31 M. H. R. Lankhorst, H. J. M. Bouwmeester and H. Verweij, *Phys. Rev. Lett.*, 1996, **77**, 2989–2992.

32 L. Wang, BSCF SOFC cathode materials: Bulk properties, kinetics and mechanism of oxygen reduction, PhD thesis, University of Stuttgart, Stuttgart, Germany, 2009.

33 M. F. Hoedl, D. Gryaznov, R. Merkle, E. A. Kotomin and J. Maier, *J. Phys. Chem. C*, 2020, **124**, 11780–11789.

34 E. Bucher, W. Sitte, G. B. Caraman, V. A. Cherepanov, T. V. Aksenova and M. V. Ananyev, *Solid State Ionics*, 2006, **177**, 3109–3115.

35 N. Grunbaum, L. Mogni, F. Prado and A. Caneiro, *J. Solid State Chem.*, 2004, **177**, 2350–2357.

36 J. Mizusaki, Y. Mima, S. Yamauchi, K. Fueki and H. Tagawa, *J. Solid State Chem.*, 1989, **80**, 102–111.

37 J. Cheng, A. Navrotsky, X. D. Zhou and H. U. Anderson, *Chem. Mater.*, 2005, **17**, 2197–2207.

38 C. Shi, H. Qin, M. Zhao, X. Wang, L. Li and J. Hu, *Sens. Actuators, B*, 2014, **190**, 25–31.

39 T. Holstein, *Ann. Phys.*, 1959, **8**, 343–389.

40 L. Friedman and T. Holstein, *Ann. Phys.*, 1963, **21**, 494–549.

41 D. Emin and T. Holstein, *Ann. Phys.*, 1969, **53**, 439–520.

42 K. J. Yoon, P. a. Zink, S. Gopalan, U. B. Pal and L. R. Pederson, *J. Electrochem. Soc.*, 2009, **156**, B795–B800.

43 J. Suntivich, W. T. Hong, Y. Lee, J. M. Rondinelli, W. Yang, J. B. Goodenough, B. Dabrowski, J. W. Freeland and Y. Shao-Horn, *J. Phys. Chem. C*, 2014, **118**, 1856–1863.

44 R. Ruhl, J. Song, V. Thore, S. P. Singh, K. Wiik, Y. Larring and H. J. M. Bouwmeester, *Phys. Chem. Chem. Phys.*, 2019, **21**, 21824–21835.

45 S. Saher, S. Naqash, B. A. Boukamp, B. Hu, C. Xia and H. J. M. Bouwmeester, *J. Mater. Chem. A*, 2017, **5**, 4991–4999.

46 H. J. M. Bouwmeester and A. J. Burggraaf, in *The CRC Handbook of Solid State Electrochemistry*, ed. P. J. Gellings and H. J. M. Bouwmeester, CRC, New York, 1997, p. 481.

47 T. Ishigaki, S. Yamauchi, K. Kishio, J. Mizusaki and K. Fueki, *J. Solid State Chem.*, 1988, **73**, 179–187.

48 J. Yoo, A. Verma, S. Wang and A. J. Jacobson, *J. Electrochem. Soc.*, 2005, **152**, A497–A505.

49 R. De Souza and J. A. Kilner, *Solid State Ionics*, 1998, **106**, 175–187.

50 A. Esquirol, J. Kilner and N. Brandon, *Solid State Ionics*, 2004, **175**, 63–67.

51 J. Mizusaki, *Solid State Ionics*, 1992, **52**, 79–91.

52 J. A. Kilner, *Solid State Ionics*, 2000, **129**, 13–23.

988 | *J. Mater. Chem. A*, 2021, **9**, 974–989

This journal is © The Royal Society of Chemistry 2021

53 J. A. Kilner and R. J. Brook, *Solid State Ionics*, 1982, **6**, 237–252.

54 M. Mogensen, D. Lybye, N. Bonanos, P. V. Hendriksen and F. W. Poulsen, *Solid State Ionics*, 2004, **174**, 279–286.

55 Z. Ogumi, K. Amezawa, M. Oishi, Y. Uchimoto, H. Arai, T. Nakao, Y. Orikasa, A. Mineshige and T. Ina, *J. Mater. Chem.*, 2011, **21**, 14013.

56 Y. A. Mastrikov, R. Merkle, E. A. Kotomin, M. M. Kuklja and J. Maier, *Phys. Chem. Chem. Phys.*, 2013, **15**, 911–918.

57 T. T. Mayeshiba and D. D. Morgan, *Solid State Ionics*, 2016, **296**, 71–77.

58 Y. L. Lee, J. Kleis, J. Rossmeisl, Y. Shao-Horn and D. Morgan, *Energy Environ. Sci.*, 2011, **4**, 3966–3970.

59 J. Hwang, Z. Feng, N. Charles, X. R. Wang, D. Lee, K. A. Stoerzinger, S. Muy, R. R. Rao, D. Lee, R. Jacobs, D. Morgan and Y. Shao-Horn, *Mater. Today*, 2019, **31**, 100–118.

60 A. M. Deml, V. Stevanović, A. M. Holder, M. Sanders, R. Ohayre and C. B. Musgrave, *Chem. Mater.*, 2014, **26**, 6595–6602.

61 J. A. Kilner, R. A. De Souza and I. C. Fullarton, *Solid State Ionics*, 1996, **86–88**, 703–709.

This journal is © The Royal Society of Chemistry 2021

J. Mater. Chem. A, 2021, **9**, 974–989 | **989**